ACS APPLIED ENERGY MATERIALS

www.acsaem.org Article

Effect of Different Bromine Sources on the Dual Cation Mixed Halide Perovskite Solar Cells

Damian Głowienka,* Francesco Di Giacomo, Mehrdad Najafi, Ilker Dogan, Alfredo Mameli, Fallon J. M. Colberts, Jędrzej Szmytkowski, and Yulia Galagan*

Cite This: *ACS Appl. Energy Mater.* 2020, 3, 8285−8294 **Read Online**

ACCESS | Metrics & More | Article Recommendations | SI Supporting Information

ABSTRACT: Recent research has shown that perovskite solar cells with a mixed dual A-cation have much better structural stability without loss of efficiency than single cation devices. Mixed cation perovskites create a lot of questions about the salts being used for the formation of the best-quality layer. Here, we have investigated three sources of bromide in the perovskite absorption layer, using lead bromide ($PbBr_2$), formamidinium bromide (FABr), and cesium bromide (CsBr). The experimental results have shown better performance for FABr and CsBr sources of bromide in comparison to the regularly used $PbBr_2$. This effect has been explained with the complex species present in the not-annealed perovskite films which changes the defect states during the crystallization of the absorber layer. It has been found with numerical simulations that the observed phenomenon directly impacts the rates of the trap-assisted recombination. The results of this study are one more step forward in understanding the physics behind the crystallization process which is crucial in further improvement of the perovskite solar cells.

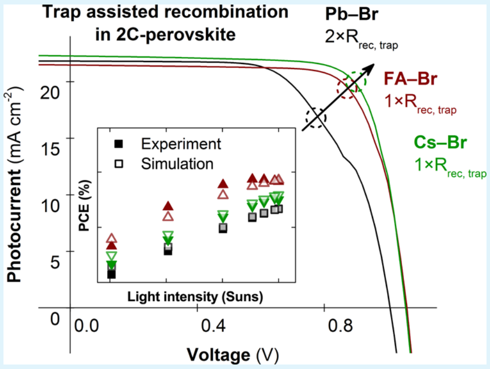

KEYWORDS: *perovskite, solar cell, bromide, bulk recombination, complex species*

■ INTRODUCTION

The perovskite materials have attracted attention in the world of photovoltaics due to rapidly improving efficiency which currently is reaching 24.2%.[1] However, the main concern for the commercialization of perovskite solar cells (PSCs) is their limited stability.[2] Therefore, recent research has led to the conclusion that PSCs with a mixed dual A-cation (2C) which consists of formamidinium and cesium ions in the perovskite layer have much better stability and efficiency.[3−5] In the same kind of perovskite material with a sufficient cesium content, it has been reported that its charge carrier properties are not reduced when increasing bromide concentration.[6] Therefore, the 2C perovskite seems to be a good candidate for application in tandem solar cells with a possibility to tune the band-gap by changing bromide and cesium content ratio,[7] especially, in the case of high efficient perovskite-based tandem solar cells.[8−11]

Using 2C perovskite in a solar cell application raises the question of which salt should be used to introduce bromine atoms. Belarbi et al.[12] have already shown that using different salts in a two-step process leads to formation of $CH_3NH_3PbBr_3$ with different morphology, optoelectronic properties, and final performance of solar cells. Also, Aldibaja et al.[13] have observed that a different source of Pb atoms might influence structural properties and solar cell performance. All this seems to be related to the precursor (colloids) solution consisting of complexes which determine the film formation and its properties.[14] Therefore, here we investigate the three sources of bromide ions in the $Cs_{0.18}FA_{0.82}Pb(I_{0.94}Br_{0.06})_3$ perovskite absorption layer, that is, lead bromide ($PbBr_2$), formamidinium bromide (FABr, where FA is a formamidinium), and cesium bromide (CsBr). The following structure lets the perovskite to be formulated with only one aforementioned source of bromide. Also, the low bromide concentration allows to omit the problems with phase segregation.[15] By keeping the same atoms and mass concentration in the precursor, we have been able to compare the same perovskite composition made from the three different bromine atom sources. We analyze the perovskite layers prepared in the p−i−n device configuration.

The goal of the following work is to understand the effect of different sources of bromide ions on the operation of the PSC. The obtained experimental results of photovoltaic parameters are analyzed with a special attention on the crystallization process which impacts the recombination via trap states. For clarity, the trap-assisted recombination is equivalently being called monomolecular recombination process in the following

Received: April 6, 2020
Accepted: July 21, 2020
Published: July 21, 2020

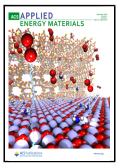

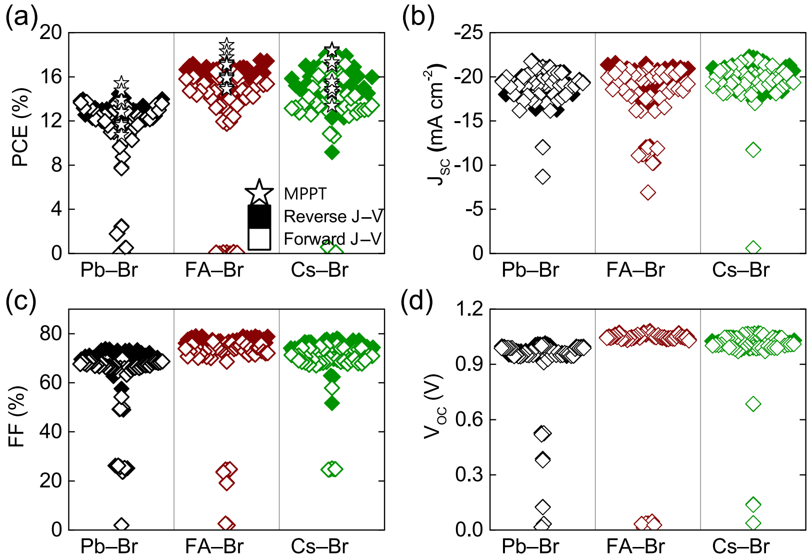

Figure 1. Photovoltaic parameters for PSCs with the effect of different bromide sources, (a) PCE, (b) J_{sc}, (c) FF, and (d) V_{oc}. Perovskites with Pb–Br (black points), FA–Br (red points), and Cs–Br (green points) as the sources of bromide.

paper. Numerical simulations have been used to study the role of different recombination rates with a drift-diffusion model which has been already applied for modeling of PSCs.[16]

EXPERIMENTAL SECTION

Device Fabrication. The precursors for the perovskite $Cs_{0.18}FA_{0.82}Pb(I_{0.94}Br_{0.06})_3$ solutions were prepared in the following manner. Commercial lead iodide (PbI_2) (99.99%, TCI), formamidinium iodide (FAI) (GreatCell Solar), cesium iodide (CsI) (99.999%, Sigma-Aldrich), lead bromide ($PbBr_2$) (99%, TCI), formamidinium bromide (FABr) (GreatCell Solar), cesium bromide (CsBr) (99.999%, Alfa Aesar), dimethylformamide (DMF) solvent (99.8%, Sigma-Aldrich), and 1-methyl-2-pyrrolidinone (NMP) solvent (99.5%, ACROS Organics) were used without further purification. For the batch to test bromide compounds with possible impurities, commercial $PbBr_2$ (99.999%, Sigma-Aldrich), $PbBr_2$ (98%, Acros Organics), FABr (>98.0%, TCI), and CsBr (99.9%, Sigma-Aldrich) were used. Three perovskite materials were prepared, called Pb–Br, FA–Br and Cs–Br, based on the single bromide source. Pb–Br was obtained by mixing the powders of 1.2 M PbI_2, 1.1 M FAI, 0.24 M CsI, and 0.12 M $PbBr_2$. FA–Br was prepared by adding 1.33 M PbI_2, 0.85 M FAI, 0.24 M CsI, and 0.24 M FABr together. Cs–Br was produced with 1.33 M PbI_2, 1.1 M FAI, and 0.24 M CsBr. The perovskite compositions were dissolved in DMF/NMP (9:1 volume ratio) solvent mixture and stirred overnight at room temperature. For the batch with the heating of the solution, the stirring temperatures were kept constant at 60, 80, and 100 °C during stirring overnight. Then, the solutions were cooled down to room temperature before spin-coating of the precursor.

The patterned glass/ITO substrates were ultrasonically cleaned and also UV–ozone treated for 30 min. The solar cells were prepared inside the glove-box with N_2 environment and the oxygen and moisture levels at about 1 ppm. First, the hole transporting layer (HTL) was spin-coated using 2 mg mL^{-1} of poly(triaryl amine) (PTAA) (Sigma-Aldrich) solution dissolved in toluene at 5000 rpm for 35 s and with the acceleration equal to 5000 rpm s^{-1}. Subsequently, the sample was annealed at 100 °C for 10 min. Furthermore, the perovskite solution was dynamically spin-coated with the gas quenching method.[17] Using 100 μL of the precursor, the two-step spin-coating program was used to acquire desired thickness: first, at 2000 rpm rotational speed for 10 s and with acceleration 200 rpm s^{-1}, and second at 5000 rpm for 30 s with 2000 rpm s^{-1}. After 15 s of spin-coating, the perovskite layer was quenched by using nitrogen gun for 15 s at 6 bars pressure with 10 cm vertical distance from the substrate. After quenching, the perovskite samples were placed immediately on the hot-plate with 100 °C for 10 min. The electron transporting layer (ETL) solution was prepared with [6,6]-phenyl C61 butyric acid methyl ester (PCBM) (99%, Solenne) material dissolved in chlorobenzene solvent to acquire 20 mg mL^{-1} solution, and further stirred overnight at 60 °C. Subsequently, the solution was spin-coated with 1500 rpm speed for 55 s and 3000 rpm s^{-1} acceleration. It was followed by spin-coating of 0.5 mg mL^{-1} bathocuproine (BCP) (99.99%, Sigma-Aldrich) solution in ethanol with 3000 rpm for 50 s and 3000 rpm s^{-1}. Afterward, the cleaning of ITO contacts was accomplished in the air with DMF/chlorobenzene solution in 1:6 volume ratio to remove all layers at the ITO contact. At last, Au electrodes were thermally deposited with shadow masks placed on top of the ETLs. The deposition was accomplished under the vacuum pressure of 1×10^{-6} mbar to acquire a thickness of 100 nm.

Characterization. The structure characterization was performed with X-ray diffractometer (XRD) (PanAlytical Empyrean). The chemical composition was analyzed by energy-dispersive X-ray (EDX) spectroscopy performed in a scanning electron microscope (Jeol JSM-6010LA IntouchScope). The morphology of the samples was investigated using scanning electron microscopy (SEM) and atomic force microscopy (AFM) (Park NX-10 tool). Fourier transformed infrared spectroscopy (FTIR) measurements were conducted using a Bruker VERTEX 70, equipped with a DLaTGS detector (350–8000 cm^{-1}). The film thickness was measured with a Bruker XT Dektak profilometer. The optical properties of the samples were investigated with an UV–vis spectrophotometer (Agilent Cary 5000) by measuring the transmittance (T) and the reflectance (R) and also with the steady-state photoluminescence (PL) spectrum (Horiba Labram Aramis system) using an excitation laser beam at 532 nm and Si detector. The current–voltage (J–V) characteristics (Keithley 2400) of PSCs were measured in N_2 conditions under a white light halogen lamp and illumination mask to define the active area of illuminated cell equal to 0.09 cm^2. The light intensity is simulating AM1.5 conditions, and therefore, it was calibrated to 100 mW cm^{-2} with a silicon reference cell. Also, a set of filters was used to obtain 1, 0.83, 0.53, 0.33, 0.1, 0.01, and 0.001 sun illumination intensities. The J–V curves were measured with a scanning rate equal to 0.165 V s^{-1} with 20 mV step without preconditioning. The scanning was performed in forward (from −0.1 to 1.1 V) and reverse (from 1.1 to −0.1 V) bias directions to analyze the hysteresis effect. The maximum power point tracking (MPPT) was measured for about 2 min with continuous illumination and also the control of voltage and current to obtain the maximum power of the solar cell. Dynamic light scattering (DLS) (Malvern Zetasizer μV) has been used to measure the hydrodynamic diameter of perovskite particles in solution. The measurements were done in plastic cuvettes at 20 °C with the 832 nm laser wavelength. The scattering angle for the measurements was 90°. DLS measures the hydrodynamic diameter for non-spherical particles. The mean particle size was calculated by integrating the intensity distribution.[18]

■ RESULTS AND DISCUSSION

The three different bromide-sourced perovskites $Cs_{0.18}FA_{0.82}Pb(I_{0.94}Br_{0.06})_3$ have been prepared in the same way but with different sources of bromide. Therefore, one perovskite is prepared with only $PbBr_2$ compound as the source of bromine atoms, second with FABr material, and third with CsBr. As it is assumed that there are no other differences, for clarity the three perovskite materials in this work are called Pb−Br, FA−Br, and Cs−Br.

The double-cation PSCs have been measured with a sun simulator at AM1.5 condition. Figure 1 shows photovoltaic parameters for 144 devices measured in reverse and forward directions to observe the effect of hysteresis. The maximum power points (MPPs) were obtained by tracking the efficiency of operating the solar cell until the steady-state conditions were identified. Figure 1a, shows that the efficiency of Pb−Br is about 3% worse in comparison to FA−Br and Cs−Br. Interestingly, the hysteresis index (HI) is different for each type of 2C PSCs.[19] It is equal to 0.056 ± 0.029, 0.073 ± 0.036, and 0.077 ± 0.036 for Pb−Br, FA−Br, and Cs−Br, respectively. Therefore, it seems that the hysteresis should be higher for FA−Br and Cs−Br samples. The higher MPPT values for FA−Br suggest the long time stability of the samples. However, the photocurrent of the three types of PSCs are about to be the same; see Figure 1b. Thus, the fill-factor (FF) and open-circuit voltage (V_{oc}) should influence the observable differences in the efficiencies. Figure 1c clearly illustrates the 6 and 5% average losses in FF for Pb−Br cells with respect to the FA−Br and Cs−Br ones, respectively. Also, the V_{oc} is lower for about 70 mV of Pb−Br solar cells; see Figure 1. The visible effect suggests the influence of bromide source on electrical properties of the investigated devices. This aspect would be further discussed in this paper.

To understand the PV effect more closely, the J−V characteristics are analyzed for the different bromide source perovskites measured for the hero solar cells; see Figure 2a. The photovoltaic parameters are also written in Table 1. These cells exhibit a low hysteresis effect and a very similar short-circuit (SC) photocurrent. The J_{sc} is more related to optical than electrical properties of the material.[20] The values of V_{oc} for FA−Br and Cs−Br are approximately the same and 70 mV higher than for the Pb−Br solar cell. The same effect has been observed for FF of the Pb−Br sample which is 12% lower than the FA−Br and Cs−Br solar cells. These observations show approximately 4% increase in power conversion efficiency (PCE) by using a different source of bromide.

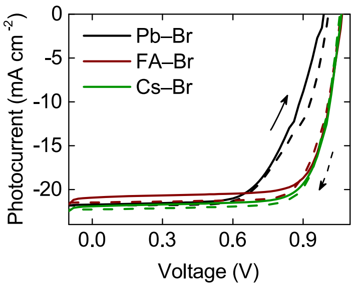

Figure 2. Experimental results for three PSCs. (a) J−V characteristics for forward (solid line) and reverse (dashed line) scans. Black, red, and green lines represent PSCs with Pb−Br, FA−Br, and Cs−Br bromide sources, respectively.

The simplest explanation could be related to possible impurities in the Pb−Br, FA−Br, and Cs−Br compounds which could influence the observed effect in solar cells. Therefore, the materials from different producers of the same compounds have been tested. Figure S1 (Supporting Information) shows results for PCE, J_{sc}, FF, and V_{oc}. It is observed that the tendencies are the same as earlier, making the Pb−Br devices about 4% worse in efficiency when compared to FA−Br and approximately 2% lower PCE than that of Cs−Br devices. More importantly, there are no differences between the different producers when analyzing the efficiency and other photovoltaic parameters. Moreover, using different purity of $PbBr_2$ from 99.999 to 98% affects the PCE negligibly. The average PCE values are equal to 10.80 ± 0.69, 10.57 ± 0.56, and 10.14 ± 0.59% based on both reverse and forward scans for the Pb−Br samples with $PbBr_2$ purity level equal to 99.999, 99, and 98%, respectively. This linear tendency confirms that the observed effect is not related to extrinsic impurities but to physical phenomena taking place in the studied solar cells.

The mass concentration of all 2C perovskites with different bromide ion sources is the same for all perovskite layers; therefore, the profilometer measurements gave the comparable thicknesses equal to 550 ± 8 nm. The thicknesses of PTAA, PCBM, and BCP layers are equal to 4.8 ± 0.5 nm, 41.0 ± 1.8 nm, and 5.2 ± 0.7 nm, respectively. The single layer of perovskite has been analyzed on the glass substrate with XRD measurements; see Figure S2a (Supporting Information). The three perovskite layers do not show any differences in diffraction patterns, suggesting that the perovskite crystals have the same crystallographic phase. The XRD results of the double-cation (2C) perovskite exhibit the regular pattern for a perovskite material with the highest intensity peaks at 14.1 and 28.3° in the (001) and (002) directions.[21] Based on the Scherrer equation, the crystallites diameters have been calculated and they are equal to 39.0 ± 1.8 nm, 43.1 ± 2.1 nm, and 39.5 ± 2.8 nm for Pb−Br, FA−Br, and Cs−Br samples, respectively. The small peaks of phase impurities are observed at 26.5 and 52.4° which are related to PbI_2 or the non-perovskite phase.[22] In general, an incorporation of FA in perovskite into A-cation leads to improvements of its electrical properties. However, the non-perovskite hexagonal phase is thermodynamically more favorable than a cubic phase in the room temperature.[23] It has been shown that an addition of Cs atoms into the perovskite stabilizes the perovskite phase.[3] Therefore, we observe perovskite layers with a negligible secondary phase. The atomic concentrations for all three $Cs_{0.18}FA_{0.82}Pb(I_{0.94}Br_{0.06})_3$ perovskites are prepared with 18% of Cs and 82% of FA in A-cation and also 94% of I and 6% of Br for the perovskite halide site. Figure S2b (Supporting Information) shows the EDX results giving the concentration of the atoms present in the 2C perovskite. As it is expected, all three perovskites have about the same concentration of the atoms. However, the samples exhibit slightly lower Cs concentration (2.1%) in comparison to the quantity used for the precursor (3.6%) which suggests that not all cesium atoms have been built in the perovskite structure. The results of EDX

Table 1. Photovoltaic Parameters for the Pb−Br, FA−Br, and Cs−Br PSCs Hero Cells

	Pb−Br		FA−Br		Cs−Br	
	forward	reverse	forward	reverse	forward	reverse
J_{sc} [mA cm^{-2}]	−21.7	−21.8	−20.9	−21.5	−21.9	−22.3
V_{oc} [V]	0.99	1.01	1.07	1.06	1.06	1.06
FF [%]	63.2	62.7	75.6	75.1	75.2	76.3
PCE [%]	13.6	13.8	16.9	17.1	17.5	18.0

imply that the bromine and iodine atoms are totally built into the structure. Figure S2c (Supporting Information) illustrates AFM pictures of surfaces which exhibit negligible differences with roughness equal to 11.2 ± 1.3, 10.4 ± 1.2, and 12.8 ± 1.5 nm, and also the average grain size equal to 125.9 ± 81.7, 113.6 ± 75.4 and 125.3 ± 85.6 nm for Pb−Br, FA−Br and Cs−Br perovskites, respectively. Figure S2d (Supporting Information) presents the SEM images which give grain size equal to 180.8 ± 21.5 nm for Pb−Br, 173.2 ± 11.3 nm for FA−Br, and 175.8 ± 7.4 nm for Cs−Br perovskite layers. Therefore, as it has been assumed, the structures of all three 2C perovskites do not show many differences.

Figure S3a (Supporting Information) illustrates optical analyzes with UV−vis measurements of single perovskite layers on the glass. It has been already shown that J_{sc} does not change much in the solar cell with a different bromide source. Here, we can see that the absorption properties are very similar to all three types of perovskite materials. Also, the results calculated from the tauc-plot give energy band-gap values equal to 1.581 ± 0.005, 1.583 ± 0.005, and 1.584 ± 0.004 eV for Pb−Br, FA−Br, and Cs−Br, respectively. Therefore, further in the paper, the approximated value of 1.58 eV for the band-gap is used for simulation purpose. Figure S3b (Supporting Information) shows the PL plots with the highest peak intensity for Cs−Br, FA−Br, and Pb−Br, respectively. The emitted photons possess an energy equal to the band-gap, and the maximum of the peak in the function of energy gives values equal to 1.605 ± 0.002, 1.601 ± 0.001, and 1.599 ± 0.001 eV for Pb−Br, FA−Br, and Cs−Br, respectively. The values are close to each other, which is the same as from the UV−vis analysis. Therefore, the optical properties of both materials are very similar with no observed differences measured so far. Also, PL is a process that is partially related to bimolecular recombination. Thus, it has been shown that a higher PL intensity in the perovskite material is related to a higher lifetime of charge carriers and therefore lowers the recombination rate.[24] This may suggest that Pb−Br has the highest recombination rate compared to Cs−Br and FA−Br. Figure S3c (Supporting Information) illustrates FTIR results of perovskite annealed films on silicon substrate. The Pb−Br sample demonstrates strong vibrational features in the range 1400−1600 cm^{-1} (C═C stretching, N−H bending, C−H bending, and N−O stretching modes) and in the range 3500−4000 cm^{-1} (mostly consisting of O−H and N−H stretching modes). Whereas the annealed Cs−Br and FA−Br films show minimal or no vibrational features in these ranges. This indicates that the molecules giving rise to these vibrational modes are less stable and free to move in Pb−Br films.

Before getting into the deeper analysis of the observed effect, its origin should be first investigated. Therefore, as the analysis of the perovskite layer does not reveal the answer, the next step is to focus on the perovskite precursor. First, we analyze the dissolution of the perovskite compounds. It is well known that heating of the perovskite solution influences the photovoltaic performance of PSC.[25−28] It has been also shown that a precursor heating may lead to the reduction of defect-mediated recombination.[27] Therefore, we have heated Pb−Br, FA−Br, and Cs−Br perovskite solutions up to 60, 80, and 100 °C before spin-coating of the solar cells. Figure 3a shows the PCE results for the aforementioned heating procedure for Pb−Br PSCs. It is observed that heating at 60 °C increases the efficiency by about 1% by mostly increasing the FF; see Figure S4b (Supporting Information). Further rise to 80 °C in temperature leads to improvement of FF to about 80% but with a negligible decrease of V_{oc} [see Figure S4c (Supporting Information)]. It seems that at 80 °C, it reaches the maximum efficiency and starts to decrease at a higher temperature which is an effect that has been also observed in the literature.[27] Figure 3b,c shows a similar behavior for FA−Br and Cs−Br. Surprisingly, the FA−Br samples seem to possess a higher hysteresis effect when temperature of the precursor is raised, as shown in Figure S4b (Supporting Information). However, most importantly, the PCE of all three types of perovskites

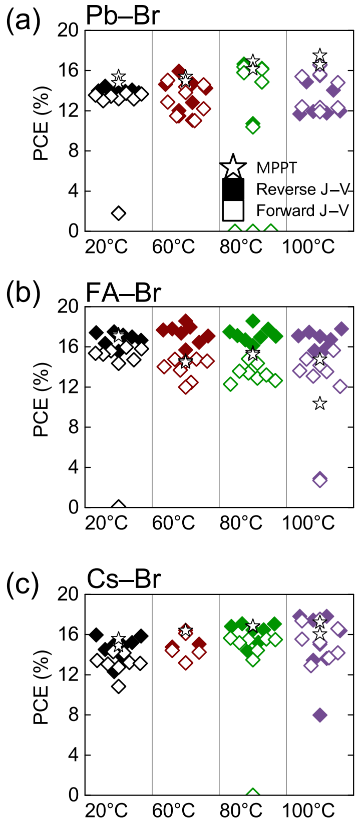

Figure 3. Photovoltaic parameters for PCE of (a) Pb−Br, (b) FA−Br, and (c) Cs−Br PSCs. Solar cells with heating of the solution overnight in 20 °C (black points), 60 °C (red points), 80 °C (green points), and 100 °C (violet points).

https://dx.doi.org/10.1021/acsaem.0c00767
ACS Appl. Energy Mater. 2020, 3, 8285−8294

have reached the same efficiency after heating of the precursors to 80 °C.

Furthermore, the regular precursors are analyzed with UV−vis and DLS methods; see Figure S5 (Supporting Information). It is already found that the perovskite precursor solution has not fully dissolved colloidal dispersions.[14] The colloids are made of organic, inorganic, and coordination compounds (complex compounds created from the formation of both organic and inorganic materials). The size and properties of the colloids determine the quality of the produced perovskite layer. The red-shift of the UV−vis absorption spectrum would suggest an increase in the colloidal size. However, the Pb−Br, FA−Br, and Cs−Br perovskite precursor spectra are not shifted; see Figure S5a (Supporting Information). Also, the DLS results show only a slight difference in the size of the observed particles; as presented in Figure S5b (Supporting Information). Therefore, the conclusion is that the diameter of colloids in perovskite precursors are approximately the same. The particle size would change if concentration of the precursor would be different.

As the precursor does not lead to any further conclusions, we decided to analyze the not-annealed perovskite films. In this work, they are also called complex or intermediate films. Such an intermediate film is strongly related to coordination effect of PbI_2 and NMP which starts to form a perovskite layer during annealing.[29] In Figure 4, XRD results are shown for complex films on a glass substrate. The not-annealed films exhibit new peaks in the range of 8−12° which are related to complex species.[30] The complex species have not been observed in the annealed perovskite films; as shown in Figure S2a (Supporting Information). At 8° there is an extra peak visible in the FA−Br and Cs−Br samples. However, it is not observed in the analyzed Pb−Br perovskite film. We have also analyzed the intermediate samples with the FTIR technique but no differences were found; see Figure S6 (Supporting Information). Also, minimal or no vibrational features are observed in the range of 1400−1600 and 3500−4000 cm^{-1}. The observed effects in the analysis of the precursor and not-annealed layer lead to the conclusion that the lower efficiency of Pb−Br solar cells should be related to properties of the complex compounds from different particles in the precursor rather than size of the colloids. Thus, it is suggested that a different source of bromide influences the type of complex compounds that are created. The colloids are nucleation seeds; thus, their properties are of great importance in the crystallization process. For a higher temperature, the solubility of all compounds is higher which leads to a more favorable situation and colloids have the same properties for all materials. The crystallization of perovskite layers has a great impact on their efficiency.[31−33] Here, it is suggested that using Pb−Br for preparation of 2C PSC without heating of the precursor leads to an increase of defect states in the absorber during the crystallization process. This is related to the rising of the trap-assisted recombination rate which lowers the operation efficiency of the devices. Furthermore, the numerical simulations would be used to confirm such an idea and help in the understanding of the role of the recombination process.

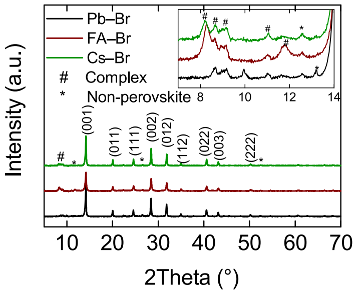

Figure 4. XRD results on glass substrate for a not-annealed perovskite layer. Perovskite with Pb−Br (black line), FA−Br (red line), and Cs−Br (green line) sources of bromide.

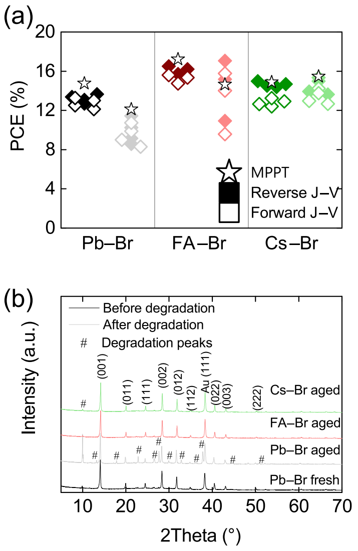

Figure 5. Experimental results for the degradation effect: (a) PCE and (b) XRD results. Fresh (dark color) and 9 months old (greyish color) samples. Perovskite with Pb−Br (black), FA−Br (red), and Cs−Br (green) sources of bromide.

Degradation analysis was performed after 9 months of storage in a nitrogen environment. The fresh samples have showed the same tendency with the worst Pb−Br samples; see Figure 5a. However, after the degradation process, the Pb−Br solar cells lost efficiency by approximately 3%. Figure S7 (Supporting Information) shows that this is due to the loss of short-circuit photocurrent and FF of the samples which has been mostly attributed to the iodine-ion migration.[34] From the other side, the FA−Br and Cs−Br has about the same efficiency with the fresh samples and the aged ones. Figure 5b shows the XRD results for the same PSCs with the fresh Pb−Br as the reference and the aged Pb−Br, FA−Br, and Cs−Br. All samples give an extra peak related to the Au electrode at 38°.[35] More importantly, the XRD spectrum of Pb−Br solar cells shows extra peaks which are related to the $CsPbX_3$ (X = I, Br) non-perovskite phase.[36,37] These extra peaks are also assigned to degradation effect as they are only observed in the aged Pb−Br sample. Figure S8 (Supporting Information) shows the SEM pictures for three different perovskites on glass. For all three samples, there are different types of crystals observed for each perovskite layer. They are mostly observed for the Pb−Br sample, where borders between two types of crystals also form a lot of pinholes; see Figure S8d (Supporting Information). Figures S9−S11 (Supporting Information) show the EDX results for the different region for Pb−Br, FA−Br, and Cs−Br samples on glass, respectively. It seems that Cs atom concentration is negligible in the Pb−Br perovskite layer, and it accumulates in the degradation crystals which supports the XRD results. A very similar behavior has been observed for the FA−Br sample but not for Cs−Br. This suggests that regularly used Pb−Br has lower stability than FA−Br and Cs−Br perovskite materials. The effect could be also related to crystal quality which is lower in Pb−Br solar cells.

For the confirmation of the hypothesis, numerical modeling of the PSCs is used. The drift-diffusion model is capable to help in finding the recombination rates when the fitting is accomplished appropriately.[38] However, the simulation of $J-V$ characteristics with this model may lead to an overestimation of the parameters due to a number of possible fitting parameters. Thus, we use the experimental results obtained for different illumination rates which give more physical variations and therefore lead to much more accurate fitting.[39]

The drift-diffusion model used in this work is described in detail in the Supporting Information. In general, the interfaces were not modified during the experiment by changing the bromide source in the perovskite precursor. Therefore, to simplify the model, it is assumed that there is no surface recombination in the PSCs. Table 2a shows the parameters presented for each layer in the PSCs stack. The layer thickness (L) of the ETL (PCBM), perovskites, and HTL (PTAA) are all measured experimentally with a profilometer. The given thicknesses are discretized with a specified number of points (N). In general, the parameters for PCBM[39−43] and PTAA[44−47] are adapted from the literature. The traps densities ($N_{\mathrm{tn(p)}}$) and trapping rates from conduction ($C_{\mathrm{nc}(\nu)}$) and valence ($C_{\mathrm{pc}(\nu)}$) bands are symmetrical and located (E_t) in the middle of the band-gap for PTAA and PCBM layers. The energy distribution for the Gaussian function in both layers is assumed to be very narrow and equal to 0.01 eV to simulate a single energy level.

Table 2. Parameters Used in Simulation of the PSCs[a]

(a) parameters used in the simulation for all used layers of the solar cells.

	unit	ETL	Perovskite	HTL
L	nm	40	550	5
N		20	100	20
ε_r		3.75	63	2.67
$\mu_{\mathrm{n(p)}}$	$\mathrm{cm^2\ V^{-1}\ s^{-1}}$	2×10^{-3}	×	(6×10^{-3})
$C_{\mathrm{nc}(\nu)}$	$\mathrm{m^3\ s^{-1}}$	10^{-18}	×	(5.88×10^{-18})
$C_{\mathrm{pc}(\nu)}$	$\mathrm{m^3\ s^{-1}}$	10^{-4}	×	(5.88×10^{-18})
$N_{\mathrm{tn(p)}}$	$\mathrm{m^{-3}}$	10^{22}	×	(10^{20})
$\Gamma_{\mathrm{n(p)}}$	$10^{-40}\ \mathrm{m^6\ s^{-1}}$	4	1.55	(4)
Ξ		10^{-4}	10^{-2}	10^{-4}
$E_{\mathrm{c}(\nu)}$	eV	−4.0	−3.9 (−5.48)	(−5.35)
$E_{\mathrm{tn(p)}}$	eV	−5.0	−4.69 (−4.69)	(−4.33)
$N_{\mathrm{D(A)}}$	$\mathrm{m^{-3}}$	10^{20}	0 (0)	(10^{20})
$N_{\mathrm{c}(\nu)}$	$\mathrm{m^{-3}}$	2.5×10^{25}	8×10^{24}	(2.5×10^{25})

(b) parameters for the simulation of the different bromide sourced perovskite layers

	unit	Pb−Br	FA−Br	Cs−Br
$\mu_{\mathrm{n(p)}}$	$\mathrm{cm^2\ V^{-1}\ s^{-1}}$	6(1)	1(0.5)	6(1)
$C_{\mathrm{nc}(\nu)}$	$10^{-14}\ \mathrm{m^3\ s^{-1}}$	10(5)	0.85(8.5)	6(25)
$C_{\mathrm{pc}(\nu)}$	$10^{-14}\ \mathrm{m^3\ s^{-1}}$	0.5(1.7)	8.5(0.85)	2(2)
$N_{\mathrm{tn(p)}}$	$10^{20}\ \mathrm{m^{-3}}$	10(20)	2(2)	4(4)

[a] For better readability, parameters for holes and electrons are written in brackets and without brackets, respectively. The parameters in (a) marked with × symbol are given in (b).

For the perovskite material, the dielectric constant (ε_r), the bimolecular recombination reduction prefactor (ξ), the Auger recombination symmetric values $\Gamma_{\mathrm{n(p)}}$, and the effective density of states $N_{\mathrm{c}(\nu)}$ are all adapted from the literature.[39,48−51] The perovskite energy bands are shifted to adjust to the band-gap acquired from the UV−vis experimental results; see Figure S3a. Table 2b shows the parameters that are varying for different bromide sources in PSCs. The mobilities are asymmetrical and within the range of the literature values.[52] It has been also found that the mobility in the FA−Br perovskite sample is lower than in Pb−Br and Cs−Br. However, this might be related to only this batch; therefore, no further conclusion is made for it. The trap densities and capture rates are obtained as a result of the fitting. Also, the trap density of states (DOS) for perovskite layers has been fixed to 0.1 eV width. The injection barriers are the Schottky barriers at the cathode/ETL and HTL/anode with values equal to 0.1 eV and 0.17 eV, respectively. The ITO material represents the anode contact, whereas BCP/Au acts as the cathode contact due to the BCP layer being a tunneling transport layer which adjusts the energy level of gold to reduce the contact losses. Therefore, these two layers could be simulated with a fixed single energy level.[53] The simulation temperature is the same as in the experiment and equal to 295 K. The built-in voltage of 1.01 V is close to the literature values.[54]

The $J-V$ characteristics have been recorded under illumination between 1 (AM1.5) and 0.001 sun (0.1% of AM1.5). There have been done measurements for 24 devices with the following method, but only the representative samples are presented here; see Figure 6. The simulated PSCs have a conversion efficiency equal to 13.65%, 16.13%, and 14.51% for Pb−Br, FA−Br, and Cs−Br, respectively. Figure 6 illustrates that the PCE increases almost linearly with illumination. Figure 6b also shows that the linear tendency of PCE is mostly due to the same relation of photocurrent. Linear relation of J_{sc} in a function of light illumination suggests the monomolecular recombination to be the dominant mechanism in SC condition.[55] The behavior of solar cell at MPP is best described with FF versus illumination intensity which is still the least understood photovoltaic parameter. Figure 6c, shows the general shape of the FF which implies a competition of two dominant recombination mechanisms. Below 0.1 sun, the FF monotonically increases for all PSCs which should be associated with the trap-assisted recombination.[56] However, below 1 sun, the FF starts to decrease slightly which may suggest that it is intrinsically related to the device structure. Figure 6d illustrates V_{oc} results plotted in a function of sun illumination. It shows logarithmic dependence on the light illumination which can be used to calculate a diode ideality factor (n_{id}) using the analytical model for V_{oc}.[57] Based on this factor, the dominant recombination mechanism can be found at an open-circuit (OC) condition. For PSC with Pb−Br, n_{id} is equal to 2.516 kT/q. Such a high value could be only explained with multiple-trapping or trap distributions.[58] The ideality factor seems to be lower for FA−Br and Cs−Br solar cells but still around 2 which suggests the trap-assisted recombination to be the dominant recombination mechanism.

Figure 6 also illustrates the simulation results for all three PSCs. The very good agreement between experimental and simulation results has been shown for the parameters from Table 2. For all samples, we can observe a small discrepancy at 0.001 sun illumination. This effect could be explained with a leakage current which has the highest impact at low intensities.[59] From the simulations for Pb−Br, it is concluded that the rate of monomolecular ($8.16 \times 10^{27}\ \mathrm{m^{-3}\ s^{-1}}$)

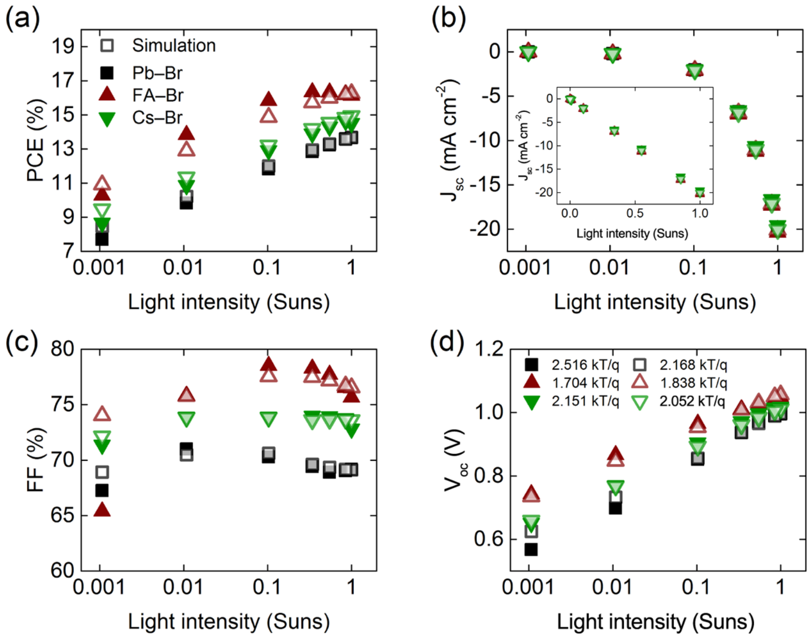

Figure 6. Photovoltaic experimental (full symbol) and simulation (open symbol) results for different illuminations: (a) PCE, (b) J_{sc} with inset having linear scale, (c) FF, and (d) V_{oc}. Solar cell structure with Pb−Br (square symbol), FA−Br (up triangle symbol), and Cs−Br (down triangle symbol) bromide source. The parameters used for simulation are shown in Table 2. 1 sun = 100 mW cm^{-2}.

recombination is about 3 orders of magnitude higher than a bimolecular rate (1.49×10^{24} m^{-3} s^{-1}) and about 10 orders higher than a trimolecular recombination rate (9.34×10^{17} m^{-3} s^{-1}) at SC. For OC, the values obtained are 4.38×10^{29}, 1.42×10^{28}, and 1.08×10^{24} m^{-3} s^{-1} for monomolecular, bimolecular, and trimolecular recombination rates, respectively. Therefore, as the monomolecular recombination was found to be dominant in all characteristics points; we further focus only on this recombination mechanism.

It has been already shown experimentally that the effect of using different bromide sources is mostly visible for FF and V_{oc}. The same is demonstrated in simulations at SC, where the difference of electric field and current density distributions is negligible; see Figure S13a,b (Supporting Information). This originates mostly from the fact that monomolecular recombination is 1 order of magnitude lower than the generation rate at SC, as shown in Figure S12a (Supporting Information). However, at MPP, it is clearly visible that an electric field within the absorber layer is the highest for Pb−Br; see Figure S13c (Supporting Information). This can be a consequence of the highest trap density which is due to the concentration of defect states created in the perovskite during the crystallization process. Therefore, the electric field impacts the total photocurrent by changing the drift of charge carriers, as shown in Figure S13d (Supporting Information). This effect is most visible in the hole partial currents which are the lowest for Pb−Br. It could be explained with the behavior of the total monomolecular recombination rate as a function of space in the device. Figure S12b (Supporting Information) shows that this rate has the highest value at the HTL side when comparing Pb−Br to two other solar cells. The total recombination rate, when integrating over a space at MPP, is about 2 times higher for Pb−Br than FA−Br or Cs−Br, as shown in Table 3. At OC, the electric field distributions are negative as we are close to built-in voltage; see Figure S13e (Supporting Information). Therefore, the absolute electric fields are misleadingly showing the highest values for FA−Br PSC. However, these values are not much different, so we can treat them as negligible variations. Thus, the observable differences in photocurrent should be related to the diffusion instead of drift currents; see Figure S13f (Supporting Information). It is expected to have zero current flowing out of the cell at OC condition which is self-consisted from simulation. However, the internal distribution may be still interrupted due to high net generation and recombination rates of charge carriers, as shown in Figure S12c (Supporting Information). Therefore, as the Pb−Br and Cs−Br have both a higher monomolecular recombination rate than a total generation rate (3.39×10^{29} m^{-3} s^{-1}), it may influence the internal total currents; see Table 3.

Table 3. Monomolecular Recombination Rates (m^{-3} s^{-1}) for the PSCs

	Pb−Br	FA−Br	Cs−Br
SC	8.16×10^{27}	2.71×10^{27}	4.12×10^{27}
MPP	7.06×10^{28}	3.93×10^{28}	4.88×10^{28}
OC	4.38×10^{29}	3.24×10^{29}	3.89×10^{29}

■ CONCLUSIONS

The study presented in this work concerned the three double-cation PSCs with Pb−Br, FA−Br, and Cs−Br bromide sources used in the PSCs. The experimental analyses have shown that Pb−Br cells have approximately 3% lower efficiency and shelf-life stability than FA−Br and Cs−Br PSCs. It has been found out that the different source of bromide influences the colloidal dispersion solutions which affects the presence of complex species in the not-annealed perovskite film. This changes the density of defect states during the crystallization of perovskite layers. The results of numerical simulations have shown that the rates of the trap-assisted recombination in Pb−Br solar cells are 2 times higher which observably impacts the operation of the solar cell. Therefore, these may find application in tandem solar cells, where the use of bromide is necessary for tuning the band-gap.

ASSOCIATED CONTENT

Supporting Information

The Supporting Information is available free of charge at https://pubs.acs.org/doi/10.1021/acsaem.0c00767.

> Photovoltaic parameters from $J-V$ curves for alternative suppliers + effect of heating solution + degradation effect; XRD data of fresh samples; EDX data of fresh + degraded samples; AFM images of fresh samples; SEM images of fresh + degraded samples; UV−vis data of fresh perovskite samples + solutions; PL data of fresh samples; FTIR data of fresh annealed + not-annealed perovskite films; DLS data of fresh perovskite solutions; and spatial simulation data of recombination rates + electric fields + photocurrents (PDF)

AUTHOR INFORMATION

Corresponding Authors

Damian Głowienka − *Faculty of Applied Physics and Mathematics, Gdańsk University of Technology, Gdańsk 80-233, Poland; TNO—Solliance, Eindhoven 5656AE, The Netherlands;* orcid.org/0000-0001-5508-2929; Email: damian.glowienka@pg.edu.pl

Yulia Galagan − *TNO—Solliance, Eindhoven 5656AE, The Netherlands; Department of Materials Science and Engineering, National Taiwan University, Taipei 10617, Taiwan;* orcid.org/0000-0002-3637-5459; Email: yulia.galagan@tno.nl

Authors

Francesco Di Giacomo − *TNO—Solliance, Eindhoven 5656AE, The Netherlands; Centre for Hybrid and Organic Solar Energy (CHOSE), Department of Electronic Engineering, University of Rome Tor Vergata, Rome 00133, Italy;* orcid.org/0000-0002-2489-5385

Mehrdad Najafi − *TNO—Solliance, Eindhoven 5656AE, The Netherlands;* orcid.org/0000-0001-6205-4838

Ilker Dogan − *TNO—Solliance, Eindhoven 5656AE, The Netherlands;* orcid.org/0000-0003-4245-787X

Alfredo Mameli − *TNO—Holst Centre, Eindhoven 5656AE, The Netherlands*

Fallon J. M. Colberts − *Molecular Materials and Nanosystems, Institute for Complex Molecular Systems, Eindhoven University of Technology, Eindhoven 5600 MB, The Netherlands*

Jędrzej Szmytkowski − *Faculty of Applied Physics and Mathematics, Gdańsk University of Technology, Gdańsk 80-233, Poland;* orcid.org/0000-0002-6494-1307

Complete contact information is available at: https://pubs.acs.org/10.1021/acsaem.0c00767

Notes

The authors declare no competing financial interest.

ACKNOWLEDGMENTS

The work has been supported by Solliance, a partnership of R&D organizations from the Netherlands, Belgium, and Germany working in thin film photovoltaic solar energy. This work is part of the research program CLEARPV, grant M-ERA.NET 2017 CW with project number 732.017.105, which is (partly) financed by the Netherlands Organisation for Scientific Research (NWO). The numerical part has also been supported by National Science Centre, Poland 2018/29/N/ST7/02326. Calculations were carried out at the Academic Computer Centre (CI TASK) in Gdańsk. The authors are grateful for the financial support for this work carried out in the "ALLSUN" project (TEUE117074) from the Dutch Ministry of Economic Affairs, via the Top-consortia Knowledge and Innovation (TKI) Program.

REFERENCES

(1) National Renewable Energy Laboratory (NREL), Chart of Best Research-Cell Efficiencies, https://www.nrel.gov/pv/assets/images/efficiency-chart.png Accessed: 2019-05-28.

(2) Correa-Baena, J.-P.; Abate, A.; Saliba, M.; Tress, W.; Jesper Jacobsson, T.; Grätzel, M.; Hagfeldt, A. The Rapid Evolution of Highly Efficient Perovskite Solar Cells. *Energy Environ. Sci.* **2017**, *10*, 710−727.

(3) Lee, J.-W.; Kim, D.-H.; Kim, H.-S.; Seo, S.-W.; Cho, S. M.; Park, N.-G. Formamidinium and Cesium Hybridization for Photo- and Moisture-Stable Perovskite Solar Cell. *Adv. Energy Mater.* **2015**, *5*, 1501310.

(4) Saliba, M.; Matsui, T.; Seo, J.-Y.; Domanski, K.; Correa-Baena, J.-P.; Nazeeruddin, M. K.; Zakeeruddin, S. M.; Tress, W.; Abate, A.; Hagfeldt, A.; Grätzel, M. Cesium-Containing Triple Cation Perovskite Solar Cells: Improved Stability, Reproducibility and High Efficiency. *Energy Environ. Sci.* **2016**, *9*, 1989−1997.

(5) Ye, F.; Yang, W.; Luo, D.; Zhu, R.; Gong, Q. Applications of Cesium in the Perovskite Solar Cells. *J. Semicond.* **2017**, *38*, 011003.

(6) Rehman, W.; McMeekin, D. P.; Patel, J. B.; Milot, R. L.; Johnston, M. B.; Snaith, H. J.; Herz, L. M. Photovoltaic Mixed-Cation Lead Mixed-Halide Perovskites: Links Between Crystallinity, Photo-Stability and Electronic Properties. *Energy Environ. Sci.* **2017**, *10*, 361−369.

(7) Bush, K. A.; Frohna, K.; Prasanna, R.; Beal, R. E.; Leijtens, T.; Swifter, S. A.; McGehee, M. D. Compositional Engineering for Efficient Wide Band Gap Perovskites with Improved Stability to Photoinduced Phase Segregation. *ACS Energy Lett.* **2018**, *3*, 428−435.

(8) Wali, Q.; Elumalai, N. K.; Iqbal, Y.; Uddin, A.; Jose, R. Tandem Perovskite Solar Cells. *Renewable Sustainable Energy Rev.* **2018**, *84*, 89−110.

(9) Zhao, D.; Wang, C.; Song, Z.; Yu, Y.; Chen, C.; Zhao, X.; Zhu, K.; Yan, Y. Four-Terminal All-Perovskite Tandem Solar Cells Achieving Power Conversion Efficiencies Exceeding 23%. *ACS Energy Lett.* **2018**, *3*, 305−306.

(10) Li, Y.; Hu, H.; Chen, B.; Salim, T.; Zhang, J.; Ding, J.; Yuan, N.; Lam, Y. M. Reflective Perovskite Solar Cells for Efficient Tandem Applications. *J. Mater. Chem. C* **2017**, *5*, 134−139.

(11) Zhao, D.; Chen, C.; Wang, C.; Junda, M. M.; Song, Z.; Grice, C. R.; Yu, Y.; Li, C.; Subedi, B.; Podraza, N. J.; Zhao, X.; Fang, G.; Xiong, R.-G.; Zhu, K.; Yan, Y. Efficient Two-Terminal All-Perovskite Tandem Solar Cells Enabled by High-Quality Low-Bandgap Absorber Layers. *Nat. Energy* **2018**, *3*, 1093−1100.

(12) Belarbi, E.; Vallés-Pelarda, M.; Clasen Hames, B.; Sanchez, R. S.; Barea, E. M.; Maghraoui-Meherzi, H.; Mora-Seró, I. Transformation of PbI_2, $PbBr_2$ and $PbCl_2$ Salts into $MAPbBr_3$ Perovskite by Halide Exchange As an Effective Method for Recombination Reduction. *Phys. Chem. Chem. Phys.* **2017**, *19*, 10913−10921.

(13) Aldibaja, F. K.; Badia, L.; Mas-Marzá, E.; Sánchez, R. S.; Barea, E. M.; Mora-Sero, I. Effect of Different Lead Precursors on Perovskite Solar Cell Performance and Stability. *J. Mater. Chem. A* **2015**, *3*, 9194−9200.

(14) Yan, K.; Long, M.; Zhang, T.; Wei, Z.; Chen, H.; Yang, S.; Xu, J. Hybrid Halide Perovskite Solar Cell Precursors: Colloidal Chemistry and Coordination Engineering Behind Device Processing for High Efficiency. *J. Am. Chem. Soc.* **2015**, *137*, 4460−4468.

(15) Hoke, E. T.; Slotcavage, D. J.; Dohner, E. R.; Bowring, A. R.; Karunadasa, H. I.; McGehee, M. D. Reversible Photo-Induced Trap Formation in Mixed-Halide Hybrid Perovskites for Photovoltaics. *Chem. Sci.* **2015**, *6*, 613−617.

(16) Głowienka, D.; Szmytkowski, J. Numerical Modeling of Exciton Impact in Two Crystalographic Phases of the Organo-Lead Halide

Perovskite ($CH_3NH_3PbI_3$) Solar Cell. *Semicond. Sci. Technol.* **2019**, *34*, 035018.

(17) Babayigit, A.; D'Haen, J.; Boyen, H.-G.; Conings, B. Gas Quenching for Perovskite Thin Film Deposition. *Joule* **2018**, *2*, 1205−1209.

(18) Colberts, F. J. M.; Wienk, M. M.; Janssen, R. A. J. Aqueous Nanoparticle Polymer Solar Cells: Effects of Surfactant Concentration and Processing on Device Performance. *ACS Appl. Mater. Interfaces* **2017**, *9*, 13380−13389.

(19) Habisreutinger, S. N.; Noel, N. K.; Snaith, H. J. Hysteresis Index: A Figure Without Merit for Quantifying Hysteresis in Perovskite Solar Cells. *ACS Energy Lett.* **2018**, *3*, 2472−2476.

(20) Ball, J. M.; Stranks, S. D.; Hörantner, M. T.; Hüttner, S.; Zhang, W.; Crossland, E. J. W.; Ramirez, I.; Riede, M.; Johnston, M. B.; Friend, R. H.; Snaith, H. J. Optical Properties and Limiting Photocurrent of Thin-Film Perovskite Solar Cells. *Energy Environ. Sci.* **2015**, *8*, 602−609.

(21) Gil-Escrig, L.; Momblona, C.; La-Placa, M.-G.; Boix, P. P.; Sessolo, M.; Bolink, H. J. Vacuum Deposited Triple-Cation Mixed-Halide Perovskite Solar Cells. *Adv. Energy Mater.* **2018**, *8*, 1703506.

(22) Zhang, M.; Yun, J. S.; Ma, Q.; Zheng, J.; Lau, C. F. J.; Deng, X.; Kim, J.; Kim, D.; Seidel, J.; Green, M. A.; Huang, S.; Ho-Baillie, A. W. Y. High-Efficiency Rubidium-Incorporated Perovskite Solar Cells by Gas Quenching. *ACS Energy Lett.* **2017**, *2*, 438−444.

(23) Lee, J.-W.; Dai, Z.; Han, T.-H.; Choi, C.; Chang, S.-Y.; Lee, S.-J.; De Marco, N.; Zhao, H.; Sun, P.; Huang, Y.; Yang, Y. 2D Perovskite Stabilized Phase-Pure Formamidinium Perovskite Solar Cells. *Nat. Commun.* **2018**, *9*, 3021.

(24) Zhang, M.; Yu, H.; Lyu, M.; Wang, Q.; Yun, J.-H.; Wang, L. Composition-Dependent Photoluminescence Intensity and Prolonged Recombination Lifetime of Perovskite $CH_3NH_3PbBr_{3-x}Cl_x$ Films. *Chem. Commun.* **2014**, *50*, 11727−11730.

(25) Khatiwada, D.; Venkatesan, S.; Adhikari, N.; Dubey, A.; Mitul, A. F.; Mohammad, L.; Iefanova, A.; Darling, S. B.; Qiao, Q. Efficient Perovskite Solar Cells by Temperature Control in Single and Mixed Halide Precursor Solutions and Films. *J. Phys. Chem. C* **2015**, *119*, 25747−25753.

(26) Zhou, H.; Chen, Q.; Li, G.; Luo, S.; Song, T.-b.; Duan, H.-S.; Hong, Z.; You, J.; Liu, Y.; Yang, Y. Interface Engineering of Highly Efficient Perovskite Solar Cells. *Science* **2014**, *345*, 542−546.

(27) Namkoong, G.; Mamun, A. A.; Ava, T. T.; Zhang, K.; Baumgart, H. Impact of Perovskite Precursor Solution Temperature on Charge Carrier Dynamics and Photovoltaic Performance of Perovskite Based Solar Cells. *Org. Electron.* **2017**, *42*, 228−233.

(28) Jung, M.; Ji, S.-G.; Kim, G.; Seok, S. I. Perovskite Precursor Solution Chemistry: From Fundamentals to Photovoltaic Applications. *Chem. Soc. Rev.* **2019**, *48*, 2011−2038.

(29) Bai, Y.; Xiao, S.; Hu, C.; Zhang, T.; Meng, X.; Li, Q.; Yang, Y.; Wong, K. S.; Chen, H.; Yang, S. a Pure and Stable Intermediate Phase Is Key to Growing Aligned and Vertically Monolithic Perovskite Crystals for Efficient PIN Planar Perovskite Solar Cells with High Processibility and Stability. *Nano Energy* **2017**, *34*, 58−68.

(30) Li, B.; Binks, D.; Cao, G.; Tian, J. Engineering Halide Perovskite Crystals Through Precursor Chemistry. *Small* **2019**, *15*, 1903613.

(31) Adhikari, N.; Dubey, A.; Gaml, E. A.; Vaagensmith, B.; Reza, K. M.; Mabrouk, S. A. A.; Gu, S.; Zai, J.; Qian, X.; Qiao, Q. Crystallization of a Perovskite Film for Higher Performance Solar Cells by Controlling Water Concentration in Methyl Ammonium Iodide Precursor Solution. *Nanoscale* **2016**, *8*, 2693−2703.

(32) Lin, Y.; Ye, X.; Wu, Z.; Zhang, C.; Zhang, Y.; Su, H.; Yin, J.; Li, J. Manipulation of the Crystallization of Perovskite Films Induced by a Rotating Magnetic Field During Blade Coating in Air. *J. Mater. Chem. A* **2018**, *6*, 3986−3995.

(33) Li, Y.; Zhi, L.; Ge, G.; Zhao, Z.; Cao, X.; Chen, F.; Cui, X.; Lin, F.; Ci, L.; Sun, J.; Zhuang, D.; Wei, J. Investigation on Crystallization of $CH_3NH_3PbI_3$ Perovskite and Its Intermediate Phase from Polar Aprotic Solvents. *Cryst. Growth Des.* **2019**, *19*, 959−965.

(34) Ginting, R. T.; Jeon, M.-K.; Lee, K.-J.; Jin, W.-Y.; Kim, T.-W.; Kang, J.-W. Degradation Mechanism of Planar-Perovskite Solar Cells: Correlating Evolution of Iodine Distribution and Photocurrent Hysteresis. *J. Mater. Chem. A* **2017**, *5*, 4527−4534.

(35) Dutta, I.; Munns, C. B.; Dutta, G. An X-Ray Diffraction (XRD) Study of Vapor Deposited Gold Thin Films on Aluminum Nitride (A1N) Substrates. *Thin Solid Films* **1997**, *304*, 229−238.

(36) Liao, J.-F.; Li, W.-G.; Rao, H.-S.; Chen, B.-X.; Wang, X.-D.; Chen, H.-Y.; Kuang, D.-B. Inorganic Cesium Lead Halide $CsPbX_3$ Nanowires for Long-Term Stable Solar Cells. *Sci. China Mater.* **2017**, *60*, 285−294.

(37) Xu, X.; Ma, C.; Xie, Y.-M.; Cheng, Y.; Tian, Y.; Li, M.; Ma, Y.; Lee, C.-S.; Tsang, S.-W. Air-Processed Mixed-Cation $Cs_{0.15}FA_{0.85}PbI_3$ Planar Perovskite Solar Cells Derived from a PbI_2−CsI−FAI Intermediate Complex. *J. Mater. Chem. A* **2018**, *6*, 7731−7740.

(38) Głowienka, D.; Zhang, D.; Giacomo, F. D.; Najafi, M.; Veenstra, S.; Szmytkowski, J.; Galagan, Y. Role of Surface Recombination in Perovskite Solar Cells at the Interface of HTL/$CH_3NH_3PbI_3$. *Nano Energy* **2020**, *67*, 104186.

(39) Sherkar, T. S.; Momblona, C.; Gil-Escrig, L.; Bolink, H. J.; Koster, L. J. A. Improving Perovskite Solar Cells: Insights from a Validated Device Model. *Adv. Energy Mater.* **2017**, *7*, 1602432.

(40) Garcia-Belmonte, G.; Munar, A.; Barea, E. M.; Bisquert, J.; Ugarte, I.; Pacios, R. Charge Carrier Mobility and Lifetime of Organic Bulk Heterojunctions Analyzed by Impedance Spectroscopy. *Org. Electron.* **2008**, *9*, 847−851.

(41) MacKenzie, R. C. I.; Kirchartz, T.; Dibb, G. F. A.; Nelson, J. Modeling Nongeminate Recombination in P3HT:PCBM Solar Cells. *J. Phys. Chem. C* **2011**, *115*, 9806−9813.

(42) Khadka, D. B.; Shirai, Y.; Yanagida, M.; Ryan, J. W.; Miyano, K. Exploring the Effects of Interfacial Carrier Transport Layers on Device Performance and Optoelectronic Properties of Planar Perovskite Solar Cells. *J. Mater. Chem. C* **2017**, *5*, 8819−8827.

(43) Juška, G.; Genevičius, K.; Nekrašas, N.; Sliaužys, G.; Dennler, G. Trimolecular Recombination in Polythiophene: Fullerene Bulk Heterojunction Solar Cells. *Appl. Phys. Lett.* **2008**, *93*, 143303.

(44) Castro-Carranza, A.; Nolasco, J. C.; Estrada, M.; Gwoziecki, R.; Benwadih, M.; Xu, Y.; Cerdeira, A.; Marsal, L. F.; Ghibaudo, G.; Iniguez, B.; Pallares, J. Effect of Density of States on Mobility in Small-Molecule N-Type Organic Thin-Film Transistors Based on a Perylene Diimide. *IEEE Electron Device Lett.* **2012**, *33*, 1201−1203.

(45) Hassan, N.; Mahmood, S. A. X-Ray Sensitivity of Poly-(triarylamine) (PTAA). *2015 IEEE International Conference on Telecommunications and Photonics (ICTP)*, 2015; pp 1−4.

(46) Tsutsumi, N.; Kinashi, K.; Masumura, K.; Kono, K. Photorefractive Performance of Poly(triarylamine)-Based Polymer Composites: An Approach from the Photoconductive Properties. *J. Polym. Sci., Part B: Polym. Lett.* **2015**, *53*, 502−508.

(47) Chen, G.; Zhang, F.; Liu, M.; Song, J.; Lian, J.; Zeng, P.; Yip, H.-L.; Yang, W.; Zhang, B.; Cao, Y. Fabrication of High-Performance and Low-Hysteresis Lead Halide Perovskite Solar Cells by Utilizing a Versatile Alcohol-Soluble Bispyridinium Salt As an Efficient Cathode Modifier. *J. Mater. Chem. A* **2017**, *5*, 17943−17953.

(48) Onoda-Yamamuro, N.; Matsuo, T.; Suga, H. Dielectric Study of $CH_3NH_3PbX_3$ (X = Cl, Br, I). *J. Phys. Chem. Solids* **1992**, *53*, 935−939.

(49) Lin, Q.; Armin, A.; Nagiri, R. C. R.; Burn, P. L.; Meredith, P. Electro-Optics of Perovskite Solar Cells. *Nat. Photonics* **2015**, *9*, 106−112.

(50) Ren, X.; Wang, Z.; Sha, W. E. I.; Choy, W. C. H. Exploring the Way to Approach the Efficiency Limit of Perovskite Solar Cells by Drift-Diffusion Model. *ACS Photonics* **2017**, *4*, 934−942.

(51) Milot, R. L.; Eperon, G. E.; Snaith, H. J.; Johnston, M. B.; Herz, L. M. Temperature-Dependent Charge-Carrier Dynamics in $CH_3NH_3PbI_3$ Perovskite Thin Films. *Adv. Funct. Mater.* **2015**, *25*, 6218−6227.

(52) Herz, L. M. Charge-Carrier Mobilities in Metal Halide Perovskites: Fundamental Mechanisms and Limits. *ACS Energy Lett.* **2017**, *2*, 1539−1548.

(53) Sakurai, T.; Wang, S.; Toyoshima, S.; Akimoto, K. Role of Electrode Buffer Layers in Organic Solar Cells. *2013 International Renewable and Sustainable Energy Conference (IRSEC)*, 2013; pp 46−48.

(54) Momblona, C.; Malinkiewicz, O.; Roldán-Carmona, C.; Soriano, A.; Gil-Escrig, L.; Bandiello, E.; Scheepers, M.; Edri, E.; Bolink, H. J. Efficient Methylammonium Lead Iodide Perovskite Solar Cells with Active Layers from 300 to 900 nm. *APL Mater.* **2014**, *2*, 081504.

(55) Giro, G.; Kalinowski, J.; Di Marco, P.; Fattori, V.; Marconi, G. Absorption Tail Photoconductivity in Solid Films of C60. *Chem. Phys. Lett.* **1993**, *211*, 580−586.

(56) Sherkar, T. S.; Momblona, C.; Gil-Escrig, L.; Ávila, J.; Sessolo, M.; Bolink, H. J.; Koster, L. J. A. Recombination in Perovskite Solar Cells: Significance of Grain Boundaries, Interface Traps, and Defect Ions. *ACS Energy Lett.* **2017**, *2*, 1214−1222.

(57) Cheyns, D.; Poortmans, J.; Heremans, P.; Deibel, C.; Verlaak, S.; Rand, B. P.; Genoe, J. Analytical Model for the Open-Circuit Voltage and Its Associated Resistance in Organic Planar Heterojunction Solar Cells. *Phys. Rev. B: Condens. Matter Mater. Phys.* **2008**, *77*, 165332.

(58) Tress, W.; Yavari, M.; Domanski, K.; Yadav, P.; Niesen, B.; Correa Baena, J. P.; Hagfeldt, A.; Graetzel, M. Interpretation and Evolution of Open-Circuit Voltage, Recombination, Ideality Factor and Subgap Defect States During Reversible Light-Soaking and Irreversible Degradation of Perovskite Solar Cells. *Energy Environ. Sci.* **2018**, *11*, 151−165.

(59) Tvingstedt, K.; Gil-Escrig, L.; Momblona, C.; Rieder, P.; Kiermasch, D.; Sessolo, M.; Baumann, A.; Bolink, H. J.; Dyakonov, V. Removing Leakage and Surface Recombination in Planar Perovskite Solar Cells. *ACS Energy Lett.* **2017**, *2*, 424−430.

■ NOTE ADDED AFTER ASAP PUBLICATION

This paper published ASAP on August 12, 2020 with an error in Yulia Galagan’s author information. The paper was revised and the correct version was reposted on August 20, 2020.

https://dx.doi.org/10.1021/acsaem.0c00767
ACS Appl. Energy Mater. 2020, 3, 8285−8294